DOI: 10.61782/fa.2025.0644

FORUM ACUSTICUM
EURONOISE 2025

ON THE ACCURACY OF THE IMAGE SOURCE METHOD IN THE PRESENCE OF TWO ADJACENT IMPEDANCE WALLS

Zeyu Xu[1*] **Emanuël A. P. Habets**[1] **Albert G. Prinn**[2]
[1] International Audio Laboratories Erlangen[†], Germany
[2] Fraunhofer IIS, Erlangen, Germany
[†]A joint institution of the Friedrich-Alexander-Universität Erlangen-Nürnberg (FAU) and Fraunhofer Institute for Integrated Circuits (IIS)

ABSTRACT

Accurate room acoustic simulations are crucial for numerous research and industrial applications, ranging from validating acoustic signal processing algorithms and training data-driven methods to virtual/augmented reality and enhancing indoor sound environments. A recent study has shown that, when compared to finite element method (FEM) benchmarks, image source method (ISM) models of arbitrarily shaped rooms can yield higher simulation errors than models of shoebox-shaped rooms. However, the underlying causes of errors remain insufficiently understood. This work focuses on a simplified yet insightful scenario: a point source near two infinite, adjoining impedance walls. By systematically varying the wall angle and the receiver position, we compare ISM-generated results against FEM solutions across different frequency ranges. Our analysis reveals potential factors driving the increased errors under these conditions, offering valuable insights for improving ISM-based approaches and guiding their application in more complex room geometries.

Keywords: *Room acoustics, image source method, finite element method, error analysis, arbitrary room geometry.*

**Corresponding author*: *zeyu.xu@audiolabs-erlangen.de.*

1. INTRODUCTION

Image Source Method (ISM) simulations, based on the assumption that sound waves propagate like light rays, encounter several challenges that can result in inaccurate room acoustics modeling. For example, the inability to accurately represent wave phenomena when either the source or the receiver is close to the walls [1], and the generation of a discontinuous sound field due to visibility issues between source images and the receiver [2]. An unaddressed issue is the inability of the standard ISM to capture some wave effects in rooms of arbitrary shape.

A room's geometry has a significant effect on the sound propagation in the room. The accuracy of the ISM has been studied for shoebox-shaped rooms, e.g., Aretz *et al.* [3] show that utilizing angle-dependent reflection coefficients can help the ISM approximate wave-based method solutions above the Schroeder frequency, and Lam [4] demonstrates that an ISM with spherical wave reflection coefficients can generate more accurate results than the standard ISM when the boundary element method is chosen as the benchmark. Borish [5] has extended the ISM from shoebox-shaped rooms to arbitrary polyhedra and introduced an image visibility test, which has been studied and implemented as a core step in utilizing the ISM for arbitrary room shapes (see, e.g., Ref. [6, 7]). More recently, Xu *et al.* [8] have extended the Diffraction-Enhanced ISM (DEISM) [9], which can model room transfer functions between transducers of arbitrary directivities, from shoebox-shaped rooms to more general room shapes. In [8], it is shown that, even for a simple room with a tilted ceiling, the ISM solution has higher errors than solutions for a shoebox-shaped room [10]. We note that error analyses of ISM models

of arbitrarily shaped rooms are lacking in the literature.

The spherical wave reflection model, see, e.g. Ref. [11], which captures the reflected sound field generated by a point source above an infinite impedance plane [1, 3, 12], is based on a plane-wave decomposition of the sound field generated by a point source image, and it can be regarded as the solution of the acoustic wave equation if the integral is computed with sufficient resolution [12]. Note that the previously mentioned ISM model with the spherical wave reflection coefficient by Lam [4] is an approximation of the full spherical wave reflection model. The spherical wave reflection model has not been included in ISM models of rooms with arbitrary geometries.

Diffraction from the edges of rooms is typically not considered in ISM models, which can lead to prediction errors. Progress in this area is limited, as there are only a few studies that investigate diffraction at the interior angles of edges. Moreover, the analytical expressions proposed in these studies are often restricted to specific cases — such as rigid or soft walls, plane-wave excitation, or integrals that are challenging to evaluate accurately [13]. It is more common to encounter edge diffraction models that focus on the exterior angles formed by two rigid walls [14–16]. In a simplified version of this problem, Calamia [2] examines a scenario involving two walls and finds that the ISM can produce a discontinuous sound field at *reflection boundaries*, which appear due to the visibility issues between the images and the receiver. However, a systematic analysis of the discrepancies between ISM and wave-based solutions of this *two-wall* problem has not yet been presented in the literature.

In this study, we examine the differences between the ISM and FEM solutions of the two-wall problem. A point source is positioned in the space created by two infinite, adjoining impedance walls. We vary the angle between the two walls and uniformly sample receiver locations within an area of interest. Our analysis focuses on the resulting distribution of errors. By investigating the patterns in these error distributions, we discuss potential causes of the discrepancies observed.

The paper is organized as follows: The considered scenario and ISM model are described in Sec. 2. The setups of the ISM and FEM simulations are presented in Sec. 3. The error analysis and discussion of possible sources of error are provided in Sec. 4. Finally, conclusions and future outlook are given in Sec. 5.

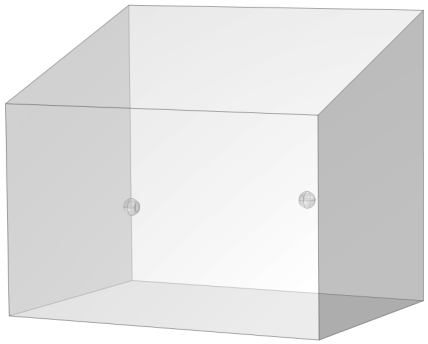

Figure 1: An illustration of a room with a tilted ceiling and two spherical-shaped loudspeakers. More details of this study can be found in Ref. [8].

2. PROBLEM FORMULATION

In Ref. [8] a room with a tilted ceiling is considered (reproduced in Fig. 1 for clarity). In that study, it is shown that the mismatch between the ISM and FEM solutions of this non-shoebox room can be as high as $10 - 20$ dB (using the log spectral distance as an error metric, which is introduced in Sec. 4.2). This level of error is significantly higher than that obtained for models of shoebox rooms.

Identifying the exact causes of errors in a room with non-shoebox geometry is not trivial, as small changes to the geometry, e.g., tilting the ceiling or enlarging the size of the room in one direction, modify the wave interference patterns. To simplify the problem, we choose a scenario, as shown in Fig. 2, for which a point source at $\mathbf{x}_\mathrm{s}$ is present in the domain constituted by two infinite walls (Wall 1 and Wall 2) separated by angle θ_W. The boundary conditions on the two walls are defined using the same frequency-independent impedance ξ for simplicity, and we assume they are locally reacting.

Following similar mathematical notations as used in [8], for a source located at $\mathbf{x}_\mathrm{s}$ and a receiver at $\mathbf{x}_\mathrm{r}$, all the reflection paths from the source to the receiver are denoted by $\mathcal{P}(\mathbf{x}_\mathrm{s}, \mathbf{x}_\mathrm{r})$. Note that the reflection paths are generated by finding the image sources and then performing a series of checks, such as validity and visibility tests [5]. For each reflection path $p \in \mathcal{P}(\mathbf{x}_\mathrm{s}, \mathbf{x}_\mathrm{r})$, the corresponding source image is located at $\mathbf{x}_\mathrm{sI}^p$. And for each mirroring operation q in the reflection path p, $\mathcal{Q}(p)$ is the set of mirroring operations and $q \in \mathcal{Q}(p)$. The reflection coefficient for the mirroring operation q in the reflection path p takes

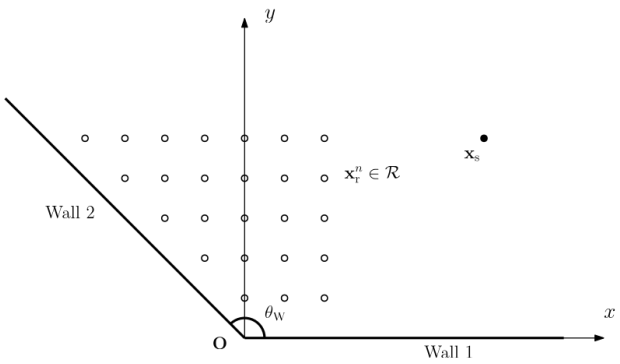

Figure 2: 2D illustration of a 3D scenario. A point source is located at $\mathbf{x}_s$ between two impedance walls, with the edge along the z axis extending toward the reader. Receiver locations $\mathbf{x}_r^n$ are evenly distributed in the x and y coordinates at the same z coordinate.

the form,

$$\beta_{p,q} = \frac{\xi \cos(\theta_{p,q}^{\text{Int.}}) - 1}{\xi \cos(\theta_{p,q}^{\text{Int.}}) + 1}\,, \tag{1}$$

where the calculation of the incident angle $\theta_{p,q}^{\text{Int.}}$ can be found in [8]. The attenuation of the reflection path p is then written as the product of sequential reflection coefficients $\beta_p = \prod_{q=1}^{Q(p)} \beta_{p,q}$. According to the ISM solution, the transfer function between the point source at $\mathbf{x}_s$ and an omnidirectional receiver located at $\mathbf{x}_r^n$, can then written as a summation of weighted Green's functions,

$$H_{\text{ISM}}(\mathbf{x}_r^n|\mathbf{x}_s, k) = \sum_{p\in\mathcal{P}(\mathbf{x}_s,\mathbf{x}_r)} \beta_p\, G(\mathbf{x}_r^n|\mathbf{x}_{sI}^p, k)\,, \tag{2}$$

where the free-field Green's function $G(\mathbf{x}_r^n|\mathbf{x}_{sI}^p, k)$ from the source image to the receiver is defined as,

$$G(\mathbf{x}_r^n|\mathbf{x}_{sI}^p, k) = \frac{e^{-ik\|\mathbf{x}_r^n - \mathbf{x}_{sI}^p\|_2}}{4\pi\|\mathbf{x}_r^n - \mathbf{x}_{sI}^p\|_2}\,. \tag{3}$$

3. SIMULATION SETUPS

The scenario under consideration is the reflection of a spherical sound wave from two walls of infinite extent that meet to form an edge. The air in the two-wall space has a speed of sound of 343 m/s and a density of 1.2 kg/m^3. A uniform frequency-independent normalized impedance [1] of $\xi = 18$ is specified at the two walls. The source position is fixed at $[1.6, 1.1, 0]$, and the receivers $\mathbf{x}_r^n$ are uniformly sampled on $x-y$ plane with $z = 0.3$ m, with a separation of 0.1 cm in the x and y directions. All points that fit in a radius of 2 m are considered. The two-wall scenario is simulated using ISM and FEM models. Both ISM and FEM solutions are generated from 20 Hz to 500 Hz, in steps of 2 Hz.

The ISM naturally models the specular reflection of sound from walls of infinite extent. The ISM model is generated using the DEISM-ARG toolbox [8, 9] by specifying the coordinates of six vertices that define finite wall approximations of the infinite walls. The coordinates are: $[0, 0, \alpha]$, $[0, 0, -\alpha]$, $[\alpha\cos(\theta_W), \alpha\sin(\theta_W), \alpha]$, $[\alpha\cos(\theta_W), \alpha\sin(\theta_W), -\alpha]$, $[\alpha, 0, \alpha]$ and $[\alpha, 0, -\alpha]$, where $\alpha = 2.5$ m. Although the toolbox is intended for a closed room, it can also simulate reflections between just two walls.

Since the FEM does not inherently model domains of infinite extent, the two walls are truncated, and the two-wall problem is modeled by two walls of finite extent. To generate the problem geometry, a semicircular plane of radius 2.6 m is extruded by an angle of θ_W to form two walls and a propagation space. To significantly reduce the levels of unwanted reflections from the domain truncation, a perfectly matched layer [17] is placed around the computational domain. Tetrahedral elements with cubic interpolating shape functions and a maximum nominal element size that ensures ten degrees of freedom per shortest wavelength are used in the computational domain. The perfectly matched layer has a depth of 0.6 m and is meshed using ten hexahedral elements. Impedance ξ is specified on both walls.

4. COMPARISONS

4.1 Distribution of the number of images

The sound ray assumption can result in a discontinuous sound field when the receiver is moved across Reflection Boundaries (RBs) or shadow boundaries [2]. The RB is a line that divides two regions with differing numbers of image sources; an image may either appear or disappear as the receiver crosses the line (depending on the direction of the movement). At the shadow boundary, the direct wave disappears (or appears, depending on direction). Since the wall angle θ_W used in this work is always less than 180°, only RBs are present here. The RBs are radius-independent in the considered scenario, and their angles can be determined from the image positions [2]. Instead

[1] The surface impedance has been normalized by the characteristic specific impedance of the air.

of finding the RBs using analytical expressions, we generate the number of visible images for each receiver position in the two-wall space, as shown in Fig. 3. Along with denoting the number of images by different colors, we also illustrate the positions of the valid source images, their mirroring order, and their generating walls in Fig. 3.

Note that valid images are determined by performing the validity test, which ensures that these images are not subsequently mirrored by the same wall. Then, the images visible at each receiver position are identified by the visibility test [5]. To highlight the RBs, lines are drawn from the valid images, through the origin, and into the two-wall space. The RBs indicate (receiver) angles at which discontinuities in the predicted sound field appear due to a changing number of visible images.

Distributions of the number of visible images at two chosen wall angles, $\theta_\mathrm{W} = 178°$ and $\theta_\mathrm{W} = 76°$, are presented in Fig. 3a and Fig. 3b, respectively. When $\theta_\mathrm{W} = 178°$, there is only one visible image in most of the domain. However, there is a narrow region between the two RBs where two images are visible. At $\theta_\mathrm{W} = 76°$, three images are visible close to the walls, but four images are visible between the two RBs. In the following, we refer to the interior region with a different number of images to its neighbors as a Reflection Boundary Region (RBR).

4.2 Distribution of log spectral distances

In this section, the differences between the ISM and FEM solutions at the receiver positions $\mathbf{x}_\mathrm{r}^n$, introduced in Sec. 3, are presented. The following error metric, viz., the root-mean-square Log Spectral Distance (LSD) [18], is calculated at each $\mathbf{x}_\mathrm{r}^n$ between wavenumbers k_1 and k_2:

$$e_\mathrm{lsd} = \sqrt{\frac{1}{K}\sum_{k=k_1}^{k_2}\left|10\log_{10}\left(\frac{|H_\mathrm{ISM}(k)|}{|H_\mathrm{FEM}(k)|}\right)^2\right|^2}, \qquad (4)$$

where K is the number of evaluated wavenumbers, and we omit the dependency of the ISM and FEM solutions on source position $\mathbf{x}_\mathrm{s}$ and receiver position $\mathbf{x}_\mathrm{r}^n$ for brevity.

In Fig. 4, we plot the distribution of the LSDs at two different frequency ranges for wall angle $\theta_\mathrm{W} = 178°$. The positions of the valid images and their mirroring orders are consistent with the ones in Fig. 3a. Additionally, the LSD distributions for $\theta_\mathrm{W} = 76°$ are shown in Fig. 5. The error metrics of the phase differences are not presented in this work, as we found them to be less informative.

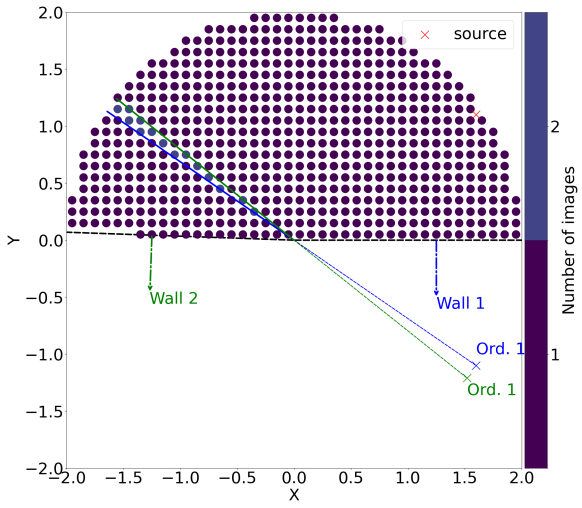

(a) $\theta_\mathrm{W} = 178°$

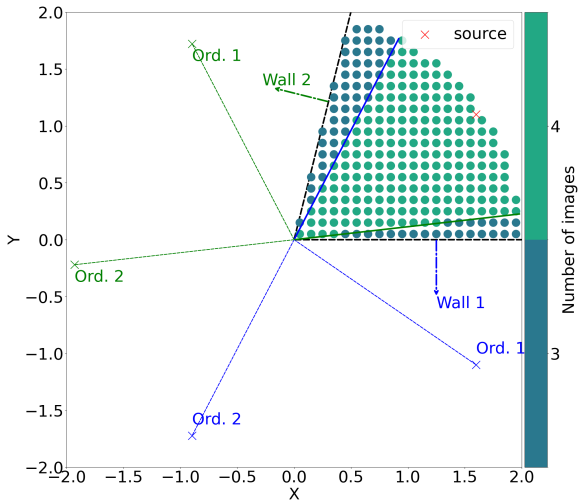

(b) $\theta_\mathrm{W} = 76°$

Figure 3: Distribution of the number of images from the source at $[1.6, 1.1, 0]$ to the receiver positions at $z = 0.3$ m for two wall angles, $\theta_\mathrm{W} = 178°$ and $\theta_\mathrm{W} = 76°$, respectively. The outward normal vectors of the two labeled walls are denoted by different colors. The source images and their mirroring orders are denoted using the same color as the normals of their generating walls. The lines extended from the connection between the images and the origin into the two-wall space denote the RBs where the number of images yields discontinuities.

4.3 Error analysis

This section analyses the errors and discusses possible causes. We divide the following analysis into two parts: analyses of the RBRs and the image numbers near RBs, which are results of the visibility test, and the missing spherical wave and diffraction effects, which are simply not modeled in the standard ISM.

4.3.1 Error discontinuity at RBs

The distributions of the LSDs for two frequency ranges, 20–30 Hz and 420–430 Hz, are presented. The frequency range 20–30 Hz is chosen since 20 Hz is the lowest frequency used in the simulation, the 10-Hz range ensures a smooth change of the LSDs over frequencies and avoids smearing the details at each frequency. The range 420–430 Hz is used here as the LSD distribution is clearly separate from the one at 20–30 Hz, and this range demonstrates typical features of the LSDs at higher frequencies (based on observations made during this study).

In Fig. 4, distinct spatial variations of the LSD are observed. The high LSD values are concentrated within the RBR, highlighting the connection between the number of images and the errors of the ISM solution. Interestingly, as discussed in [2], the RBs forming the RBR are also the singularities of the diffraction term used in Biot-Tolstoy-Medwin (BTM) Diffraction Formulation [14–16].

It is worth mentioning that the RBs always exist regardless of whether an interior or exterior edge is formed by the two adjoining walls. However, when $\theta_W > 180°$ only one RB is present, while when $\theta_W < 180°$ multiple RBs caused by multiple reflection orders may be present. For the specific angle $\theta_W = 178°$, shown in Fig. 4, the two walls are close to forming a single larger wall. Since only one image is usually required for the ISM when a point source is above a planar surface, we have two closely spaced source images from the two walls, leading to a possible error in the generated sound field.

The sound pressure levels (SPLs) and phase responses of the ISM and FEM solutions at $\mathbf{x}_r^1 = [-0.35, 0.25, 0.3]$, which has the maximum LSD of 2.48 dB (darkest color in Fig. 4a), are compared in Fig. 6. We observe a near-constant shift in SPLs of around 3 dB between the ISM and FEM solutions. This is caused by the additional (spurious) image source in the RBR. Comparing only the reflected fields (not presented in this paper), a difference of approximately 6 dB is found, indicating a doubling of pressure caused by the superposition of two closely spaced point sources. In contrast, the SPLs and phase re-

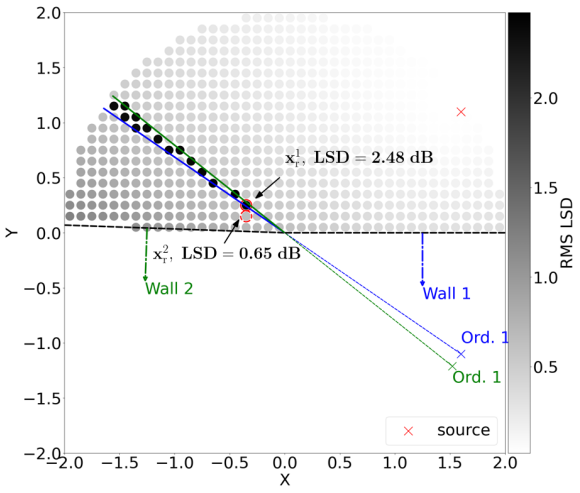

(a) Averaged from 20 Hz to 30 Hz.

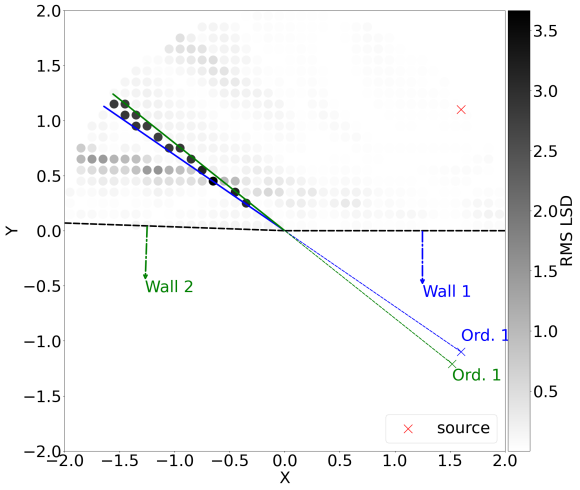

(b) Averaged from 420 Hz to 430 Hz.

Figure 4: Distribution of the LSDs at the receiver positions for angle $\theta_W = 178°$ for two frequency ranges. The two closely-spaced first-order images generated by each wall form an RBR with two images instead of one, as shown in Fig. 3a. The RBR exhibits higher LSDs compared to the neighboring regions. Receivers at $\mathbf{x}_r^1$ and $\mathbf{x}_r^2$ illustrated in Fig. 4a are used for analysis in Fig. 6.

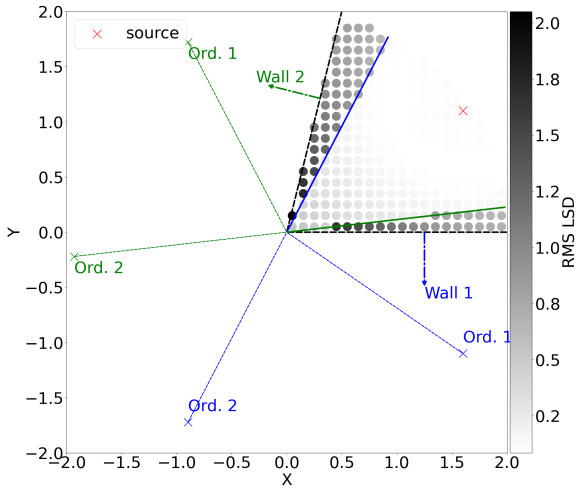

(a) Averaged from 20 Hz to 30 Hz.

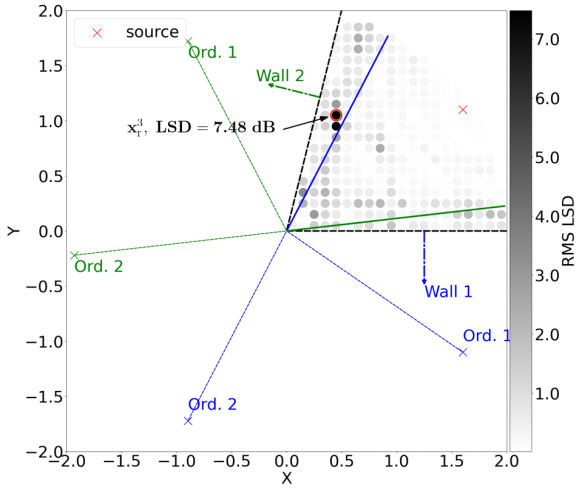

(b) Averaged from 420 Hz to 430 Hz.

Figure 5: Distribution of the LSDs at the receiver positions for angle $\theta_W = 76°$. The RBR contains one more image than the neighboring regions. The correlation between the distribution of image number and the distribution of high LSD values is more prominent at lower frequency ranges, which is different from observations in Fig. 4. The maximum value of the LSDs has increased to 7.48 dB.

sponses of the FEM and ISM solutions at receiver position $\mathbf{x}_r^2 = [-0.35, 0.15, 0.3]$, which is outside of the RBR, are compared in Fig. 6. In this case, the SPLs of the two solutions are in agreement.

We now consider the case of $\theta_W = 76°$, for which the numbers of visible images are shown in Fig. 3b. There is one less image in the two regions on either side of the RBR. This leads to lower LSDs in the RBR at lower frequencies, as shown in Fig. 5a. However, at higher frequencies, see Fig. 5b, the LSD values do not align with the regions delineated by the RBs. This is in contrast to the pattern observed in Fig. 4b. This implies that large LSDs, some as high as 7 dB, are not caused solely by changes in the number of images.

4.3.2 Missing wave effects

Returning to Figs. 4a and 4b, apart from the high LSD values in the RBR, we also observe an additional lower level of errors, which is not related to the RBs.

At lower frequencies, the LSD values increase when the receiver is closer to the walls, especially when closer to the left edge of the left wall, as shown in Fig. 4a. This could be attributed to the omission of spherical wave effects in the reflected sound field, an error that is more prominent at lower frequencies. Aretz *et al.* [3] demonstrate the difference between the standard ISM and the spherical wave reflection model by varying the surface impedance, the specular reflection angle, and the sum of the heights of the receiver and the image relative to the infinite surface divided by the wavenumber. Their analysis shows that the standard ISM could lead to high errors when the source and, or, receiver approach a surface due to the method's inability to model spherical wave reflections, especially at lower frequencies. Considering the data shown in Fig. 6a, we observe that at very low frequencies, below approximately 50 Hz, both ISM solutions disagree with the FEM solutions. Combining this with the observation made of Fig. 4a above, this low-frequency disagreement is expected to be caused by the omission of spherical wave reflection coefficients in the ISM.

Another possible cause of error is the omission of edge diffraction effects (see, e.g., [2, 13, 16, 19]). In Fig. 7, we present the SPLs and phase responses of the ISM and FEM solutions at the receiver position $\mathbf{x}_r^3 = [0.45, 1.05, 0.3]$ for $\theta_W = 76°$, which corresponds to the highest LSD value (7.48 dB) in Fig. 5b. Note that this receiver is close to but outside of the RBR. In contrast to the SPLs shown in Fig. 6, the differences between the SPL solutions manifest as changes in the locations of the dips.

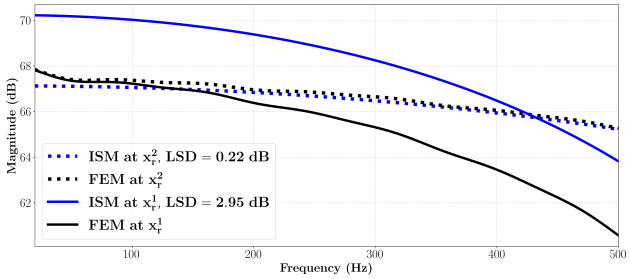

(a) Sound pressure levels.

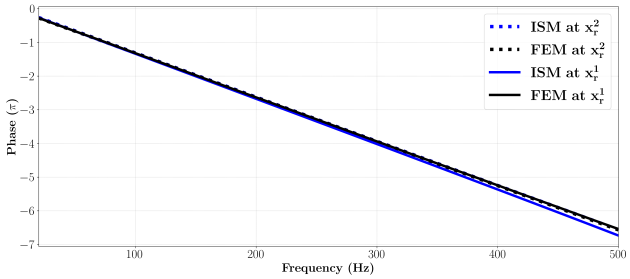

(b) Phase response.

Figure 6: The SPL and phase response at all frequencies at receiver location $\mathbf{x}_r^1 = [-0.35, 0.25, 0.3]$ in the RBR and a closely spaced location at $\mathbf{x}_r^2 = [-0.35, 0.15, 0.3]$ outside the RBR for $\theta_W = 178°$. The two receiver locations are also depicted in Fig. 4a. The corresponding LSDs in the whole frequency range are 2.95 dB and 0.22 dB, respectively. For the former receiver location, one can observe a nearly consistent shift of the SPLs between the ISM and FEM solutions while the phase responses start to diverge at higher frequencies. While for the latter receiver location, the ISM and FEM solutions are nearly consistent.

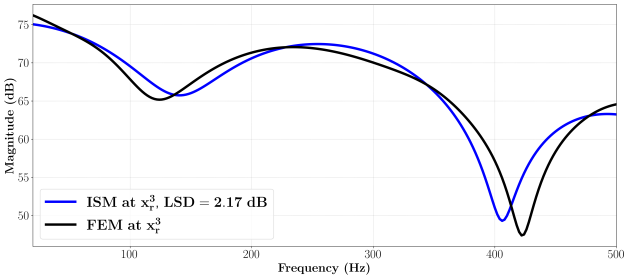

(a) Sound pressure levels.

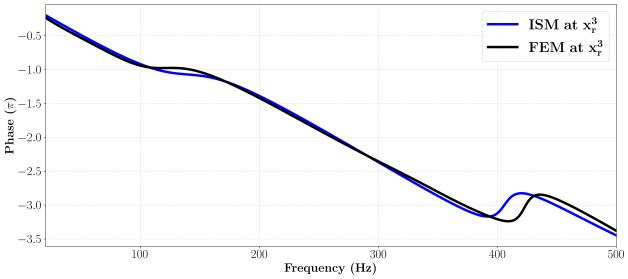

(b) Phase response.

Figure 7: The SPL and phase response at all frequencies at receiver location $\mathbf{x}_r^3 = [0.45, 1.05, 0.3]$ for $\theta_W = 76°$. This receiver location corresponds to the position with maximum LSD (highlighted by red circle) in Fig. 5b. The most significant difference between the ISM and FEM solution appears to occur at higher frequency ranges, viz., a shift of the dip in the SPL responses.

The phase responses at the frequencies of the two dips (the one around 140 Hz is less sharp) also shift accordingly. Calamia [2] investigates a similar scenario, where a point source is present in a rigid-walled two-wall problem with $\theta_W = 75°$. He compares the difference of the BTM diffraction model for receivers on either side of an RB and shows that the two diffraction contributions have opposite polarities.

Returning to the present work, it is expected that the observed differences are caused mainly by the omission of edge diffraction in the standard ISM. However, a demonstration of this is not presently available due to the unavailability of a closed-form solution for interior edge diffraction from two infinite impedance walls.

Based on these observations, we hypothesize that the error of standard ISM models of rooms with arbitrary geometries may consist of three components:

1. the presence, or absence, of images caused by a visibility test that considers only specular reflections,
2. the omission of spherical wave reflection effects, and,
3. the omission of edge and corner diffraction effects.

Proposing models that mitigate these sources of error is a subject for future work.

5. CONCLUSIONS

In this work, we have analyzed the differences between the ISM and FEM solutions of a simple scenario in which a point source generates a sound field in the space formed by two adjoining infinite impedance walls. We considered the distributions of the number of images and the distributions of error over a plane of receivers, and we compared the transfer functions at specific positions of interest.

We have shown that, in some cases, the distribution of the error aligns with the distribution of the number of images. This demonstrates that the visibility test used in the ISM could lead to the presence or absence of source images that pollute the sound field. We have also discussed other possible sources of error, i.e., the omission of spherical wave reflection effects and the omission of edge diffraction effects, which are typically not modeled in the standard ISM.

The analysis carried out in this work serves as an initial study of the error distribution and the possible sources of error in very simple cases. In practice, the error of the standard ISM depends implicitly on room geometry, source and receiver positions, and surface impedance. A sophisticated and systematic analysis of the errors is required to determine the exact contributions of sources of error for a given set of model input parameters.

6. REFERENCES

[1] F. Mechel, "Improved mirror source method in room acoustics," *J. Sound Vib.*, vol. 256, no. 5, pp. 873–940, 2002.

[2] P. T. Calamia, *Advances in Edge-Diffraction Modeling for Virtual Acoustic Simulations*. PhD thesis, Princeton University, NJ, 2009.

[3] M. Aretz, P. Dietrich, and M. Vorländer, "Application of the mirror source method for low frequency sound prediction in rectangular rooms," *Acta Acust. united Acust.*, vol. 100, no. 2, pp. 306–319, 2014.

[4] Y. W. Lam, "Issues for computer modelling of room acoustics in non-concert hall settings," *Acoust. Sci. Technol.*, vol. 26, no. 2, pp. 145–155, 2005.

[5] J. Borish, "Extension of the image model to arbitrary polyhedra," *J. Acoust. Soc. Am.*, vol. 75, pp. 1827–1836, June 1984.

[6] D. Schröder, *Physically based real-time auralization of interactive virtual environments*. PhD thesis, RWTH Aachen, 2011.

[7] Pyroomacoustics 0.7.4, "Room simulation." `https://pyroomacoustics.readthedocs.io/en/pypi-release/pyroomacoustics.room.html`, 2024. Accessed: 2024-05-07.

[8] Z. Xu, E. A. P. Habets, and A. G. Prinn, "Simulating sound fields in rooms with arbitrary geometries using the diffraction-enhanced image source method," in *2024 18th International Workshop on Acoustic Signal Enhancement (IWAENC)*, pp. 284–288, 2024.

[9] Z. Xu and E. A. P. Habets, "audiolabs/deism: New directivity profiles and examples," Dec. 2024.

[10] Z. Xu, A. Herzog, A. Lodermeyer, E. A. P. Habets, and A. G. Prinn, "Simulating room transfer functions between transducers mounted on audio devices using a modified image source method," *J. Acoust. Soc. Am.*, vol. 155, pp. 343–357, Jan. 2024.

[11] L. Brekhovskikh, *Waves in layered media*, vol. 16. Elsevier, 2012.

[12] J. S. Suh and P. A. Nelson, "Measurement of transient response of rooms and comparison with geometrical acoustic models," *J. Acoust. Soc. Am.*, vol. 105, no. 4, pp. 2304–2317, 1999.

[13] F. Mechel, *Room acoustical fields*. Springer Science & Business Media, 2012.

[14] M. A. Biot and I. Tolstoy, "Formulation of Wave Propagation in Infinite Media by Normal Coordinates with an Application to Diffraction," *J. Acoust. Soc. Am.*, vol. 29, pp. 381–391, Mar. 1957.

[15] H. Medwin, "Shadowing by finite noise barriers," *J. Acoust. Soc. Am.*, vol. 69, no. 4, pp. 1060–1064, 1981.

[16] U. P. Svensson, R. I. Fred, and J. Vanderkooy, "An analytic secondary source model of edge diffraction impulse responses," *J. Acoust. Soc. Am.*, vol. 106, no. 5, pp. 2331–2344, 1999.

[17] J.-P. Berenger, "A perfectly matched layer for the absorption of electromagnetic waves," *J. Comput. Phys.*, vol. 114, no. 2, pp. 185–200, 1994.

[18] A. Gray and J. Markel., "Distance measures for speech processing," *IEEE Trans. Acoust, Speech, Signal Process.*, vol. 24, no. 5, pp. 380–391, 1976.

[19] A. D. Pierce, *Acoustics: an introduction to its physical principles and applications*. Springer, 2019.